Determination of the crystal structures in the A-site ordered YBaMn$_2$O$_6$ perovskite.

Javier Blasco,[a] Gloria Subías,[a] José Luis García-Muñoz,[b] François Fauth,[c] and Joaquín García,[a]*

[a] Instituto de Nanociencia y Materiales de Aragón (INMA), CSIC-Universidad de Zaragoza, and Departamento de Física de la Materia Condensada, Universidad de Zaragoza, C/ Pedro Cerbuna 12, 50009 Zaragoza, Spain. [b] Institut de Ciència de Materials de Barcelona, ICMAB-CSIC, Campus UAB, 08193, Bellaterra, Spain. [c] CELLS-ALBA Synchrotron Light Source, 08290 Cerdanyola del Vallès, Barcelona, Spain.

CORRESPONDING AUTHOR'S EMAIL:

jbc@unizar.es

ABSTRACT

We present a complete structural study of the successive phase transitions observed in the YBaMn$_2$O$_6$ compound with layered ordering of cations on the perovskite A-site. We have combined synchrotron radiation x-ray powder diffraction and symmetry-adapted modes analysis to describe the distorted structures as pseudosymmetric with respect to the parent tetragonal structure. The YBaMn$_2$O$_6$ compound shows three consecutive phase transition on cooling from 603 K down to 100 K. It undergoes a first order structural transition at T$_1 \approx$ 512 K from a $C2/m$ cell with a single Mn site to $P2_1/c$ cell with two non-equivalent Mn sites. No checkerboard ordering of the two types of MnO$_6$ octahedra is revealed and there is not significant charge segregation. A second transition is observed below T$_2 \approx$ 460 K giving rise to a duplication of the c axis and the occurrence of four non-equivalent Mn sites. These sites are grouped in two pairs producing in this case a checkerboard arrangement in the ab plane with an average charge segregation of $\Delta q \approx$ 0.4 e$^-$. The observed distortions in this phase disagree with the formation of an orbital ordered phase. Finally, another structural transition is observed coupled to the magnetic transition at T$_N \approx$ 200 K and the c axis is no longer duplicated. The low temperature phase is polar with SG $P2_1$. It also contains four non-equivalent Mn sites grouped in two pairs. The charge difference between these pairs is increased achieving a value of $\Delta q \approx$ 0.7 e$^-$. In this phase, an asymmetric stretching mode favors a Jahn-Teller-like distortion in the expanded MnO$_6$ octahedra that could be associated with an ordering of e_g ($3d_{x^2-z^2}/3d_{y^2-z^2}$) orbitals. Our refinements disclose that this phase is ferroelectric with significant polar displacements of the Mn and O$_{basal}$ atoms along the b axis. The simultaneous occurrence of ferroelectricity and magnetic ordering indicates that YBaMn$_2$O$_6$ can be considered as a type II multiferroic compound and can present magnetoelectric coupling.

INTRODUCTION

Manganese perovskites have been the subject of intense research due to the close interplay between magnetism and current transport properties that gives rise to exotic phenomena such as giant magnetoresistance or charge ordering (CO) phases.[1-3] The rich phase diagram of these compounds promises a wide variety of applications that include for example suitable materials for solid oxide fuel cell,[4] oxygen storage,[5] multifunctional spintronic,[6] or solid state refrigeration.[7] The origin of these fascinating properties is the competitive interactions among spin, charge, orbital and lattice degrees of freedom which are especially strong in half doped manganites where different CO and orbital ordering (OO) phases are stabilized.[8-11] More recently, the strong impact that A-site order has on these properties has been found.[12-14] In these compounds with nominal formula $RBaMn_2O_6$ (R=rare earth or Y), the A-site ordering makes the MnO_2 sublattice sandwiched between the RO and BaO sublattices of very different sizes inducing asymmetric distortions in the MnO_6 octahedron.[12] Furthermore, the combination of A-site ordering and MnO_6 octahedral tilt can break inversion symmetry through the trilinear coupling mechanism giving rise to new type of hybrid-improper ferroelectricity.[15] As manganites usually exhibit strong magnetic interactions, this mechanism opens the possibility of developing new multiferroic materials whose application is more promising due to the success in the epitaxial growth of thin films.[16]

In the case of large R atoms (La, Pr and Nd) the ferromagnetic (FM) correlations are enhanced in A-site ordered compounds with respect to the parent simple perovskites.[12,13,17] The ground state of $LaBaMn_2O_6$ exhibits a long range ferromagnetic order with the typical tetragonal cell of an undistorted A-site ordered perovskite.[17,18] In the case of Pr- and Nd-based compounds,

the FM transition is followed by an antiferromagnetic (AFM) ordering coupled to a metal-insulator-like transition.[18-21] In both cases there is neither CO nor OO in the low temperature phase which is orthorhombic and polar with a single site for the Mn atoms.[18,21]

The situation differs for compounds with smaller R atoms. CO phases are strengthened and the phase transition temperature, T_{CO}, increases with decreasing the R-size.[12] It is noteworthy that the corresponding polymorph compounds with disorder in the A-site, $R_{0.5}Ba_{0.5}MnO_3$ (R=Pr-Eu and Y) do not exhibit neither CO nor long range magnetic ordering.[22,23] Thus, the ordering of R and Ba atoms in the perovskite structure leads to the reduction of electrostatic potential disorder that favors the high ordering temperatures in $RBaMn_2O_6$ compounds for both, CO and magnetic transitions. The ground state of the CO phase is characterized by an AFM ordering of CE-type and the occurrence of $(h/4, k/4, l)_T$ superstructure peaks respect to the parent tetragonal cell.[13] In the case of $SmBaMn_2O_6$ compound, there are two non-equivalent Mn sites at first ascribed to Mn^{3+} and Mn^{4+} ions with the former site displaying an ordered distortion attributed to an OO of e_g ($3d_z^2$-$_r^2$) orbitals.[6] When heating, there is a temperature range where $(h/4, k/4, l/2)_T$ superstructure peaks are observed and they were ascribed to a change in the stacking sequence of the OO along the **c** axis.[14,20,24-26] Similar change in the OO was reported for compounds with smaller R cations.[27] Our recent symmetry-adapted modes analysis of $SmBaMn_2O_6$ have revealed that charge segregation between the non-equivalent Mn sites is indeed below the nominal separation of one charge unit. The local environments of the two types of Mn atoms are distorted showing anisotropy in both CO phases, but only in the low temperature CO phase one of the distorted MnO_6 octahedron resembles a Jahn-Teller like distortion.[28]

The study of the $YBaMn_2O_6$ (YBMO) compound is of great interest because it has the highest T_{CO} in the $RBaMn_2O_6$ series and a complete structural characterization is still missing. In

the first studies of YBMO, it was identified that it had three transitions as a function of temperature.[13,29] A first order structural transition at T_1=520 K accompanied by a sudden drop of the magnetization. Then, a metal-insulator transition is observed at T_{MI}=480 K and an AFM ordering at T_N=190 K. At T_1, the crystal structure changes from a pseudo tetragonal cell ($T>T_1$) to a pseudo orthorhombic one ($T<T_1$) but with monoclinic symmetry in both cases. No ($h/4$, $k/4$, l)$_T$ superstructure peaks are identified in these studies.[13,29] Another study[27] using transmission electron microscopy (TEM) detected superstructure peaks at RT corresponding to two propagation vectors: q_1= (¼, ¼, 0)$_T$ and q_2= (0, 0, ½)$_T$. These peaks were not observed in neutron powder diffraction (NPD) measurements on the same specimen. The occurrence of both superstructure peaks is associated to the formation of a checkerboard CO in the *ab* plane coupled to an OO whose orientation changes every two MnO$_2$ layers along the **c** axis. A stacking sequence AABB along this direction is deduced for the OO phase at RT and the actual lattice parameters should be $2\sqrt{2}a_T \times \sqrt{2}a_T \times c_T$ (referred to the ideal tetragonal structure). The same group analyzed the NPD data of YBMO at different temperatures. A triclinic structure with symmetry P1 and $\sqrt{2}a_T \times \sqrt{2}a_T \times c_T$ is proposed for T= 580 K > T_1. Cooperative tilts of the MnO$_6$ octahedra following the tilt system $a^0b^-c^-$ in the Glazer's terminology[30] is proposed as the main component to stabilize this high temperature phase.[31] For T=500 K<T_1, the tilts system changes to $a^-b^-c^-$ and the resulting structure is monoclinic with space group (SG) *P2* and similar lattice parameters with respect to the parent tetragonal cell. TEM measurements did not reveal ($h/4$, $k/4$, $l/2$)$_T$ or ($h/4$, $k/4$, l)$_T$ superstructure peaks at high temperature and it was ascribed to the loss of oxygen at 500 K. The same *P2* structure remains at 350 K where the ($h/4$, $k/4$, $l/2$)$_T$ and ($h/4$, $k/4$, l)$_T$ superstructure peaks are appreciated by TEM but not by NPD.[31] Therefore, this monoclinic cell can be considered an average of the actual structure and the distortions that give rise to the ($h/4$, $k/4$, $l/2$)$_T$ or ($h/4$, $k/4$, l)$_T$ peaks remain

undetermined. It is also quite intriguing that all the structures deduced by this study are non-centrosymmetric and compatible with the development of ferroelectricity.

Williams et al.[32] carried out a crystallographic study of YBMO between RT and 773 K. At the highest temperature, YBMO is orthorhombic crystallizing in the SG *Cmmm*, isostructural to $SmBaMn_2O_6$. At 523 K ($T>T_1$), the compound is monoclinic and the SG is *C2/m* with a single site for Mn atoms. The lattice parameters of this monoclinic cell are $2\mathbf{a}_T \times 2\mathbf{a}_T \times \mathbf{c}_T$. This result is in contradiction with the previous study.[31] Finally, Williams et al.[32,33] resolved the crystal structure of YBMO below T_1 using a triclinic cell with SG *P-1*, also in contradiction with the study by Nakajima et al.[31] In this centrosymmetric structure with lattice parameters $\sqrt{2}\mathbf{a}_T \times \sqrt{2}\mathbf{a}_T \times \mathbf{c}_T$, there are two non-equivalent Mn sites with a charge segregation that are assigned to a checkerboard arrangement of Mn^{3+} and Mn^{4+} cations. The bond lengths calculated suggest a Jahn-Teller distortion in the Mn^{3+}-site that are oriented parallel in the *ab* plane. This result was interpreted as a new type of ferro-OO of e_g ($3d_z^2$-$_r^2$) orbitals.[33] It is noteworthy that the present structure also does not explain the ($h/4$, $k/4$, $l/2$)$_T$ peaks seen by TEM, which suggests that the YBMO structure may be more complex.

Summarizing, several structural approaches have been reported for YBMO, some of them contradictory, but a complete solution that accounts for all the observed superstructure peaks is still missing. For this purpose, we have carried out a comprehensive structural study of YBMO using synchrotron x-ray powder diffraction (SXRPD). This technique minimizes problems arising from twinning, multiple scattering and self-absorption and allows us to map the temperature dependence of the crystal structure with high accuracy. In order to recognize the distortions associated with a specific structural transition we have used the symmetry-adapted modes. In this way, we have analyzed the different structures as distortions of the ideal parent tetragonal structure

identifying the primary distortion modes responsible of each transition. Our study discloses the existence of two consecutive CO phases at low temperature but only one of them presents a Jahn-Teller-like distortion compatible with an OO of e_g ($3d_{x^2-z^2}/3d_{y^2-z^2}$) orbitals. The latter phase is developed in a polar phase and the phase transition temperature concurs with the magnetic transition suggesting the possibility of a strong magnetoelectric coupling. Therefore, YBMO can be considered as a type II multiferroic compound.

MATERIALS AND METHODS

Stoichiometric amounts of dried Y_2O_3, $BaCO_3$ and Mn_2O_3 were mixed, ground and heated at 1000ºC overnight. The resulting powder is reground, pressed into pellets and sintered at 1250ºC in a gas flow of H_2/Ar mixture (2 % of H_2) saturated in water vapor to achieve a reductive atmosphere ($P_{O2} \approx 10^{-11}$). This is required to prevent the formation of $BaMnO_3$ impurity.[17] Thus, the pellets are reground, pressed into pellets and sintered at 1375ºC for 24h in the same atmosphere. After this step, the material is oxygen deficient, $YBaMn_2O_{5+\delta}$ with $\delta \approx 0.1$. The next step consists of a topotactic oxidation at 450ºC in an oxygen current flow for 24 h yielding the stoichiometric $YBaMn_2O_6$ compounds.

Rietveld analysis of the x-ray patterns were performed using the Fullprof package program[34] with the symmetry-mode analysis. The input file with the basis modes was obtained from the AMPLIMODES program[35] from Bilbao Crystallographic server. AMPLIMODES/SYMMODES and ISODISTORT programs,[36] were used to explore the different distorted structures of the YBMO compound. The schematic illustrations of the crystal structures were obtained with the VESTA program.[37]

The chemical composition of the powders was also tested using wavelength dispersive x-ray fluorescence spectrometry (Advant'XP+ model from Thermo-ARL) and the Y:Ba:Mn stoichiometry agreed with the expected values within the experimental error (1%).

SXRPD patterns were measured at the MSPD beam line[38] of the ALBA synchrotron (Cerdanyola del Vallès, Spain) using high-throughput position sensitive detector MYTHEN which accommodates of very high photon flux necessary to detect minor superstructure peaks. The samples were loaded in a borosilicate glass capillary (diameter of 0.5 mm) and kept spinning during data acquisition. A short wavelength, $\lambda=0.4128$ Å, was selected to reduce absorption. The value of λ was determined using a NIST standard silicon. A FMB Oxford hot air blower is coupled close to the capillary to perform measurements between RT and 603 K while an Oxford cryostream was additionally coupled to measure patterns between 100 and 440 K. There is a temperature range of around 140 K where patterns were collected using both experimental settings and no difference was observed. We have performed two types of measurements. Standard patterns to refine unit cell parameters were collected in heating and cooling ramps between 100 and 440 K (using cryostream and hot air blower), and between RT and 603 K (using the hot air blower only). The rate was 0.5 K.min^{-1} and the total acquisition time was 6 min. With this procedure, we collected a pattern every 3 K on average. Secondly, SXRPD patterns with high statistics were measured at selected temperatures (100, 303, 440, 503 and 603 K) with a total acquisition time of 30 min./pattern to perform a full structural characterization of the different phases found in YBMO.

Magnetic measurements were carried out with a commercial Quantum Design (SQUID) magnetometer. The dc magnetization was measured between 5 and 700 K with an external field of 1 kOe.
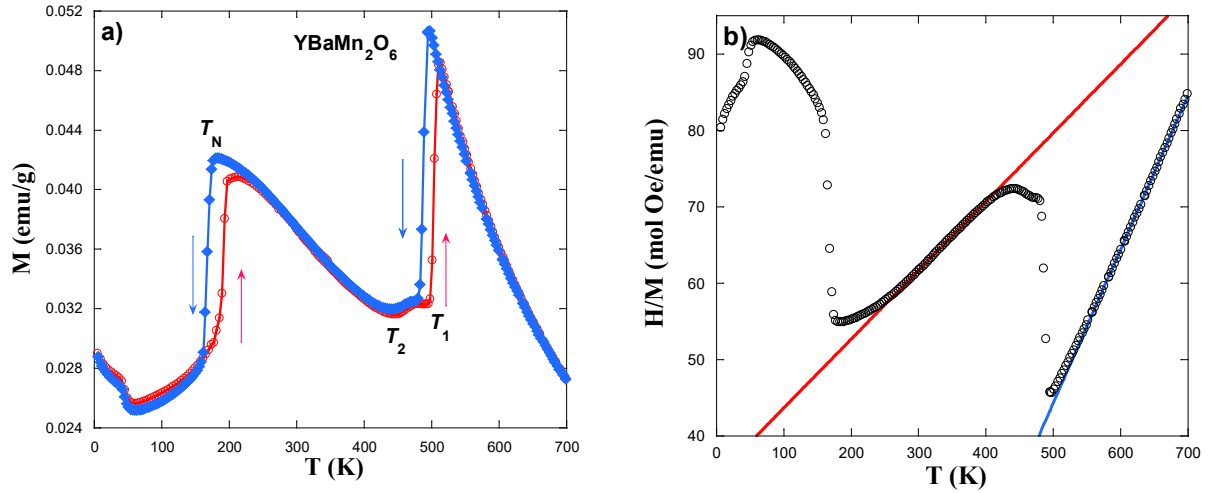
Figure 1. (a)Temperature dependence of the magnetization for $YBaMn_2O_6$ at 1 kOe by heating (red circles) and cooling (blue diamonds) the sample as indicated by the arrows. (b) Inverse of magnetization vs. temperature in the cooling run. The straight lines show the fits to a Curie-Weiss law in two ranges of the experimental data.

RESULTS AND DISCUSSION

Figure 1(a) represents the temperature dependence of the magnetization for YBMO between 5 and 700 K. Overall, the M(T) curve agrees with those reported in previous studies.[13,29] In this way, the magnetization shows a sudden drop in the temperature range between 495 and 512 K depending on whether the sample is heated or cooled. This feature relates to the structural transition at T_1 and the thermal hysteresis agrees with a first order transition. Below this drop, there is a small and rounded anomaly at $T_2 = 450$-460 K that matches the reported temperature for the metal-insulator transition.[13,29] Below this anomaly, the magnetization increases with decreasing temperature down to 173 K in cooling conditions (or 198 K in the heating run) where a second sudden drop in the M(T) curve is observed. This temperature concurs with the expected one for the magnetic transition, T_N, and the AFM ground state is CE-type.[27] The occurrence of thermal hysteresis

suggests that the magnetic ordering may be coupled to a first order structural transition. Above the magnetic transition, this compound exhibits two different paramagnetic regimes. Fig. 1(b) shows the inverse of magnetic susceptibility (cooling run) and two linear regions following a Curie-Weiss law can be observed. At high temperature and above the metal-insulator transition the fit to a Curie-Weiss law yields the following parameters: C= 5.024 emu K/mol, θ= 275 K and ρ_{eff}= 6.33 μ_B/fu. The effective paramagnetic moments match quite well the expected ones from the spin only contribution of an even mixture of Mn^{3+} and Mn^{4+} cations, ρ_{theo}= 6.24 μ_B/fu. The positive sign of the Weiss constant (θ) indicates the presence of ferromagnetic correlations in this paramagnetic regime. Below the structural transition at T_1, the fit to a Curie-Weiss law can be performed between 250 and 390 K. The refined parameters are: C= 11.11 emu K/mol, θ= -385.7 K and ρ_{eff}= 9.42 μ_B/fu. In this case ρ_{eff} is much higher than the theoretical value indicating strong correlations between the Mn moments in this temperature region. In addition, the sign of θ is now negative indicating a change in the sign of the dominant magnetic correlations that are now AFM. Finally, a small increase in magnetization is observed below 50 K in Fig. 1 (a). This may be due to a small canting of the magnetic arrangement but a contribution of a small fraction of A-site disordered phase, $Y_{1/2}Ba_{1/2}MnO_3$, that behaves as a spin-glass like phase,[22] is also a plausible explanation. In order to account for the impact of the disordered phase, magnetic measurements of YBMO and $Y_{1/2}Ba_{1/2}MnO_3$ are compared in the supplementary section. From the value of low temperature magnetization, we have estimated a fraction of 0.9% *wt.* of $Y_{1/2}Ba_{1/2}MnO_3$ as maximum in our sample. This tiny contribution has negligible effects on the hysteresis loops (see supplementary information) or SXRPD patterns (see later on).
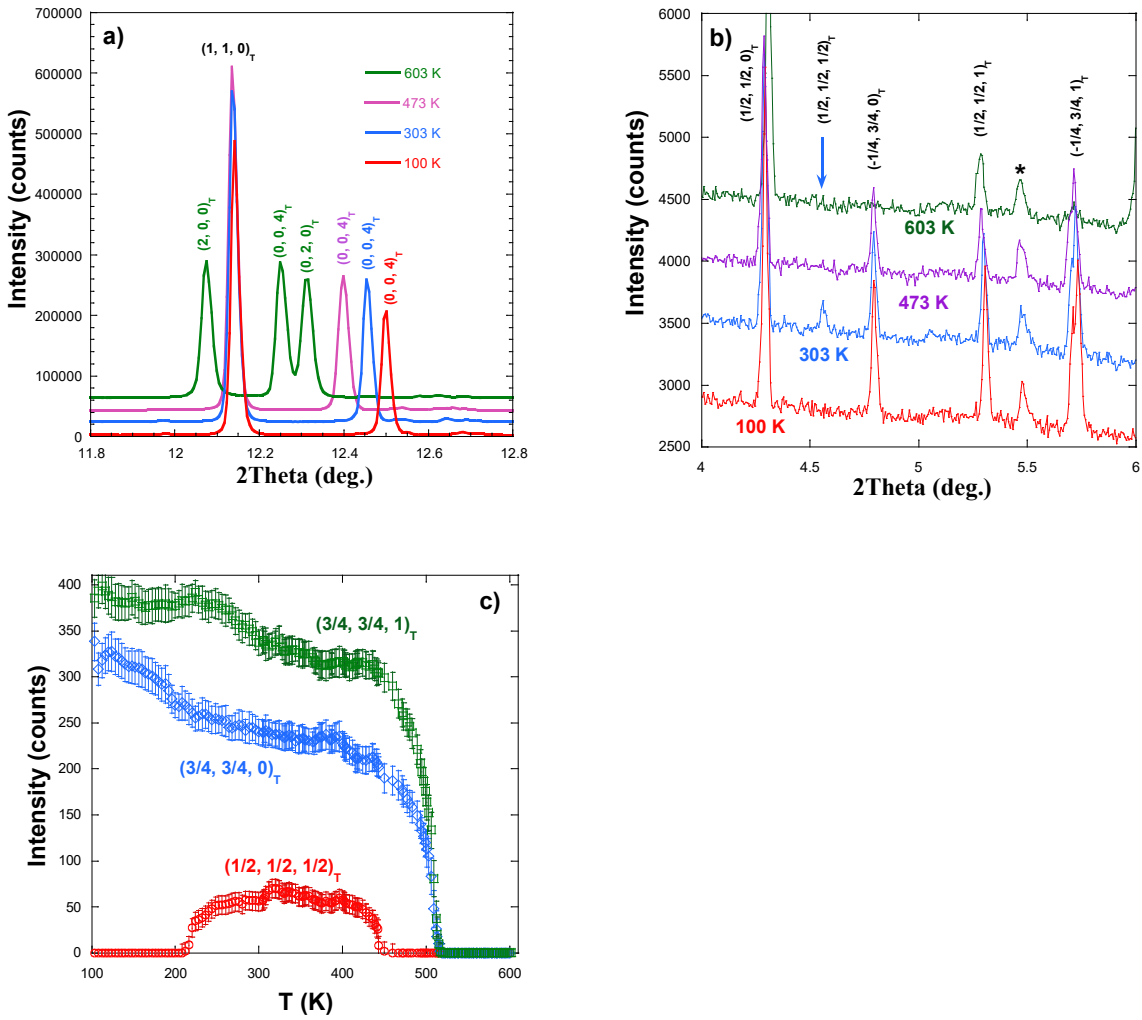
Figure 2. Details of the SXRPD patterns showing (a) the changes of the splitting in main diffraction peaks indicating a unit cell change, and (b) the occurrence of different superstructure peaks at different temperatures. The asterisk marks the main peak of the secondary phase Y_2O_3 (0.3% in wgt.). (c) Temperature dependence of selected superstructure peaks. The subscript T in all panels indicates that indexation of the peaks is related to the parent tetragonal cell.

Strong changes are also observed in the SXRPD patterns when varying the temperature. Fig. 2 compares two sections of the patterns collected at four distinct temperatures and the main

differences are observed in the splitting of fundamental reflections (Fig. 2(a)) and in the appearance of different families of superstructure peaks (Fig. 2(b)). At 603 K (well above T_1), the splitting of the $(h, 0, 0)$ reflections respect to the parent tetragonal cell reveals the doubling of the a and b axes. In addition, only $(h/2, k/2, 0)_T$ superstructure peaks are observed in the patterns and all of the peaks can be indexed using the $2\mathbf{a}_T \times 2\mathbf{a}_T \times \mathbf{c}_T$ cell parameters. At 473 K (below T_1), the $(h, 0, 0)_T$ and $(0, k, 0)_T$ reflections are replaced by the $(h, h, 0)_T$ one and new $(h/4, k/4, l)_T$ superstructure peaks appear in the pattern. The whole pattern can be indexed using the $2\sqrt{2}\mathbf{a}_T \times \sqrt{2}\mathbf{a}_T \times \mathbf{c}_T$ cell parameters. At 303 K (below T_2), an additional set of $(h/2, k/2, l/2)_T$ superstructure peaks are noticeable in the SXRPD patterns indicating the doubling of the c axis at this temperature (Fig. 2(a),(b)). Therefore, the pattern can be indexed using the $2\sqrt{2}\mathbf{a}_T \times \sqrt{2}\mathbf{a}_T \times 2\mathbf{c}_T$ cell. Finally at the lowest temperature tested (100 K, below T_N), the $(h/2, k/2, l/2)_T$ superstructure peaks have vanished and the lattice parameters are again $2\sqrt{2}\mathbf{a}_T \times \sqrt{2}\mathbf{a}_T \times \mathbf{c}_T$.

Fig. 2(c) shows the temperature dependence of representative superstructure peaks (in heating conditions) where it is appreciated how the peaks $(h/4, k/4, l)_T$ and $(h/2, k/2, l/2)_T$ have different origins. The former appear at 515 K, close to the temperature of the first magnetic anomaly seen in the M(T) curve (Fig. 1(a)), and remain in the patterns down to 100 K. The second ones are visible below 450 K, close to low temperature limit of the second rounded anomaly observed in the Fig. 1(a). This peak disappears at 210 K, close to the magnetic transition temperature.[27] Below this temperature, it is visible a slight increase in the intensity of the $(h/4, k/4, l)_T$ peaks with even l while the intensity remains almost constant for odd l. Similar features for the superstructure peaks were reported for the related compound $SmBaMn_2O_6$ and it was ascribed to a change of the OO ordering from AABB to AAAA with decreasing temperature.[25] According to the magnetic properties and the temperature dependence of the superstructure peaks, we have

selected several temperatures to acquire SXRPD patterns with high statistics in order to solve the crystal structures of YBMO between 100 and 603 K. We have taken full advantage of the full symmetry mode analysis to relate each distorted phase to the parent tetragonal phase of the undistorted perovskite with SG *P4/mmm*.

Crystal structure at high temperature (T>T$_1$, metallic-like phase). The SXRPD pattern at 603 K can be indexed in a C-centered monoclinic unit cell in agreement with ref. 32. Along with this main phase, very small peaks corresponding to the cubic phase of Y_2O_3 are also seen in the pattern (0.3% in *wgt* as determined from Rietveld refinement). This phase was also included in all refinements. Regarding the occurrence of A-site disordered phase (see magnetic study), we have not detected evidence of its presence in the SXRPD patterns. One possibility is that this phase is poorly crystallized giving rise to broad diffraction peaks that are masked by the background. Another option is the occurrence of anti-site defects at the A-site producing an intrinsic disorder in our specimen. In order to check this point, fraction occupancies of Y and Ba have been refined in both sites preserving the nominal stoichiometry. The refined occupancies yield values of 98(1)% Y + 2(1)% Ba at the Y-site (and *vice versa* for the Ba-site) but the improvement in the reliability factors of the fit is negligible, so the A-site order of our specimen can be considered almost perfect. The monoclinic cell at high temperature, whose SG is *C2/m*, can be considered as a distorted structure of the parent tetragonal phase with lattice vectors (2,0,0)$_T$, (0,2,0)$_T$ and (0,0,-1)$_T$ with an origin shift of (1/2, 0, -1/2). According to the formalism of distortion modes,[35,39] this monoclinic phase can be pictured as the superposition of modes ascribed to irreducible representations (irreps) of the ideal *P4/mmm* structure.[17,18] A total of 16 individual modes are allowed in the distortion of the *P4/mmm* structure into the *C2/m* one. They are grouped in six irreps as follows: GM1+(2), GM2+(1), GM5+(3), M3-(3), M4-(1) and M5-(6) where capital letters stand for the associated

points in the first Brillouin zone of the primitive tetragonal cell and the numbers in parenthesis indicate the dimension of each irrep or its number of individual modes. This structural model yields accurate fits as can be seen in the supplementary section, and the refined parameters are summarized in the Table 1. Fig. 3 compares the ideal tetragonal structure with the distorted monoclinic structure The mode analysis is also included in the supplementary information. The primary modes of this distorted structure belong to the irreps M5- and M4- and corresponds to tilts of MnO_6 octahedra that are responsible of the occurrence of $(h/2, k/2, l)_T$ superstructure peaks. The tilt system is $a^-b^0c^-$ in the Glazer's terminology,[30] *i.e.* it corresponds to antiphase rotations of the octahedra along two orthogonal directions. The modes belonging to the irrep M4- are responsible of the rotation around the c axis involving the four basal oxygens (O2) and can be considered as a tilt of rigid MnO_6 octahedra. However, the modes from M5- produce the rotation around the a axis with differences between the displacements of basal and apical oxygens and between both types of apical oxygens. The reason is the different steric effect produced by the big Ba^{2+} and the small Y^{3+} cations. For this reason, MnO_6 octahedra can no longer be considered rigid. The rest of the modes belonging to other four irreps have a much smaller amplitude and play a secondary role in the stabilization of the monoclinic cell. In this cell, the Mn atoms occupy a single site in the lattice and the bond valence sum method[40] gives a value of +3.41(1), i.e. this atom is a bit underbonded in this structure. However, the main structural strain is located at the A-sites, the calculated valence for Ba and Y atoms is +2.39(1) and +2.43(1), respectively. This implies that Ba^{2+} is significantly overbonded in this cell while Y^{3+} is strongly underbonded. The strain produced by the small size of Y^{3+} is relieved by the cooperative tilts indicated previously and can be considered as the driven force for the formation of this monoclinic structure.

Table 1. Structural parameters of YBaMn$_2$O$_6$ obtained from Rietveld refinement at 603 K.

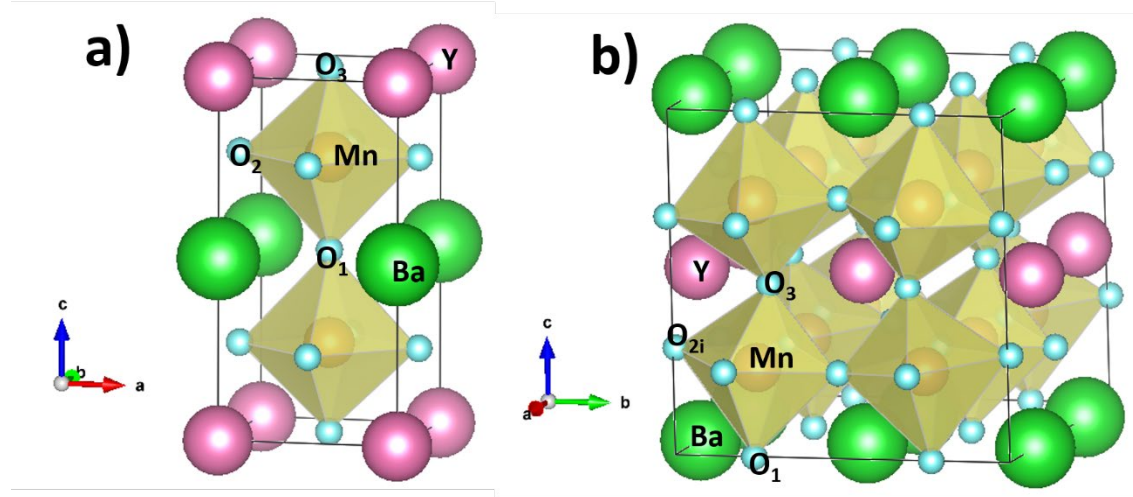|	Atom	Pos.	x	y	z	B_{iso}(Å^2)
SG: *C2/m*						
a = 7.85525(4) Å	Y	*4i*	0.2603(2)	0	0.5021(2)	1.15(2)
b = 7.70467(3) Å	Ba	*4i*	0.2523(1)	0	0.0018(1)	1.06(1)
c = 7.74282(3) Å	Mn	*8j*	0.0003(2)	0.2496(2)	0.2577(1)	0.77(1)
β = 90.2894(1)	O1	*4g*	0	0.2358(11)	0	0.5(1)
V = 468.606(4) Å^3	O2$_1$	*4i*	-0.0295(9)	0	0.3047(8)	1.1(1)
R$_p$ (%) = 3.4	O2$_2$	*4i*	0.5256(9)	0	0.2517(8)	1.1(1)
R$_{wp}$ (%) = 5.1	O2$_3$	*8j*	0.2501(6)	0.2256(7)	0.2870(5)	1.6(1)
R$_{Bragg}$(%) = 2.9	O3	*4h*	0	0.2932(8)	½	0.7(1)
χ^2 = 2.4						

Figure 3. (a) Crystal structure of the ideal tetragonal structure of YBMO. (b) Crystal structure of YBMO at 603 K adopting the monoclinic cell with space group *C2/m*. O$_1$ and O$_3$ stand for apical oxygens while O$_{2i}$ refer to basal oxygens (i=1-3, see Table 1)

Crystal structure at 473 K (T$_1$>T>T$_2$, charge disordered insulating phase). New superstructure peaks indexed as (h/4, k/4, l)$_T$ occurs below T$_1$. The new lattice has the following parameters: 2√2a$_T$×√2a$_T$×c$_T$, *i.e.* the new *a* and *b* axes are along the diagonal of the primitive tetragonal lattice and one of the diagonals is duplicated. This type of distorted cells is usually ascribed to the combination of CO and OO.[2] We have used the Isodistort tool[36] to explore the

possible distorted structures able to account for the new superstructure peaks. These peaks arise from distortions associated to the k-point (¼, ¼, 0) that belongs to the SM line in the first Brillouin zone of the primitive tetragonal lattice. Since the same $(h/2, k/2, l)_T$ superstructure peaks remain in the pattern collected at 473 K, the search was focused on possible structures driven by the combination of modes belonging to the irreps M5-, M4- and SM. The solutions were limited to those that were in accordance with the abovementioned lattice parameters. The possible solutions are summarized in the supplementary information. Among the candidate solutions, triclinic groups can be ruled out because the corresponding splitting of fundamental reflections have not been detected in the pattern. The systematic absence of (h, k, l) reflections with $k+l$=odd seems to point to the $P2_1/c$ SG. We have tested this possibility obtaining an accurate fit as can be seen in the supplementary information. The lattice parameters of the monoclinic cell, referred to the parent structure, are $(0, 0, 1)_T$, $(2, -2, 0)_T$ and $(-1, -1, 0)_T$ and the origin shift is $(1, -1/2, 0)$. It is noteworthy that the axes a and c are interchanged in the monoclinic cell with respect to the tetragonal one and the unique axis is along the doubled axes in the ab plane. Table 2 summarizes the refined parameters and Fig. 4 shows the crystal structure. In the $P2_1/c$ structure there are two non-equivalent Mn sites but the BVS method yield similar valences in both sites: 3.47(3) and 3.40(3) for Mn1 and Mn2, respectively. This implies that $C2/m \rightarrow P2_1/c$ transition does not produce any significant charge segregation in the Mn sublattice which remains however a bit underbonded. There is not a checkerboard arrangement of the two MnO_6 octahedra but a dimer distribution as can be seen in the Fig. 4(a) (forming stripes parallel to c that alternate along the a axis). The mode decomposition of the structural refinement can be seen in the supplementary information. The primary modes correspond to the irreps M5-, M4- and SM2 whereas the rest of modes are secondary and in particular, the modes belonging to the irreps GM5+ and M1- are negligible. The

distortions associated to the irreps M4- and M5- correspond to the abovementioned tilts of the

MnO_6 octahedron. Along with them, we have the distortions associated with the irrep SM2 that

are responsible for the occurrence of the $(h/4, k/4, l)_T$ peaks. These modes include a set of atomic

displacements that make different the environments of the two non-equivalent Mn sites. The set

of atom shifts induced by these distortions modes can be viewed in the Fig. 4(b). With regard to

the basal oxygens, it is of interest that these active modes only act on half of them. In this way,

one mode rotates two basal oxygens leading to in-phase shift of a pair of O2 atoms in the *bc* plane.

Another mode produces a twist distortion in the other pair of O2 atoms with small displacements

along the *a* axis in opposite directions as indicated in Fig. 4(b).

Table 2. Structural parameters of YBaMn₂O₆ obtained from Rietveld refinement at 473 K.

	Atom	Pos.	x	y	z	$B_{iso}(Å^2)$
SG: $P2_1/c$						
	Y	*4e*	-0.0073(3)	0.6305(1)	0.7478(3)	0.84(2)
a = 7.65059(2) Å	Ba	*4e*	0.4959(2)	0.6259(1)	0.7564(2)	0.93(1)
b = 11.05070(3) Å	Mn1	*4e*	0.2409(2)	0.6264(3)	0.2617(3)	0.94(5)
c = 5.52690(1) Å	Mn2	*4e*	0.2431(2)	0.1244(3)	0.2407(3)	0.30(3)
β = 90.3043(1)	O1	*4e*	-0.0021(9)	0.6536(6)	0.3056(13)	0.77(13)
V = 467.262(2) Å³	O2₁	*4e*	0.1956(9)	0.4900(4)	0.0268(8)	1.18(5)
	O2₂	*4e*	0.2381(9)	0.7599(7)	0.4999(14)	1.18(5)
R_p (%) = 3.0	O2₃	*4e*	0.2048(9)	-0.0100(4)	0.0268(8)	1.18(5)
R_{wp} (%) = 4.6	O2₄	*4e*	0.2339(9)	0.2619(7)	0.4504(14)	1.18(5)
R_{Bragg}(%) = 2.4	O3	*4e*	0.4968(13)	0.6126(7)	0.2451(18)	0.65(10)
χ^2 = 2.0						

Instead, the Ba atom continues being strongly overbonded (BVS=+2.74) while Y one is

less underbonded (+2.61) respect to the *C2/m* phase. Based on these data, it seems that this

distortion tends to stabilize the environment of the Y^{3+} cation at the expense of destabilizing the

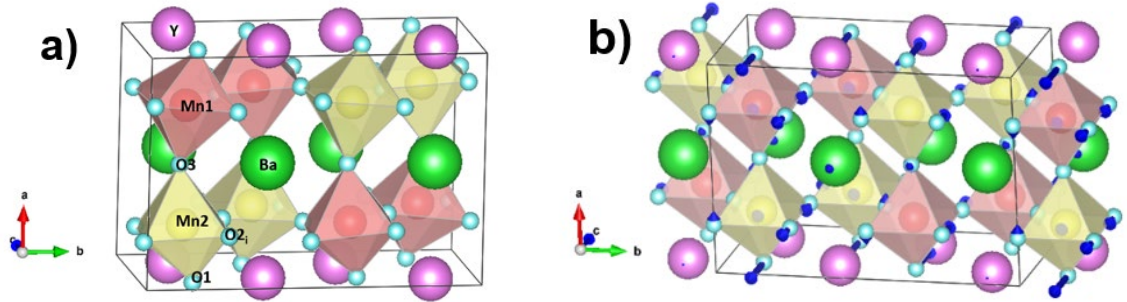Ba^{2+} site, which now supports the greatest structural strain.

Figure 4. (a) Crystal structure of YBaMn$_2$O$_6$ at 473 K. (b) Representation of the atomic shifts produced by the distortion modes belonging to the irrep SM2.

Crystal structure of the HT-CO phase at 303 K (T$_2$>T>T$_N$). Two sets of superstructure peaks coexist at this temperature: $(h/4, k/4, l)_T$ and $(h/2, k/2, l/2)_T$. Accordingly, the new lattice parameters accounting for all diffraction peaks is $2\sqrt{2}\mathbf{a}_T \times \sqrt{2}\mathbf{a}_T \times 2\mathbf{c}_T$. Following the same strategy as in the previous section, we have used the Isodistort tool to explore distortions arising from the combination of the previous main modes (M4-, M5- and SM2) and distortions associated to the k-point (½, ½, ½). Among the possible solutions, one catches our attention. It's a monoclinic cell with SG *P2$_1$/n* (No. 14, standard setting *P2$_1$/c*). The reason is that its symmetry is closely related to an analogous phase of the SmBaMn$_2$O$_6$ compound.[28] Both compounds exhibit related structural phase transitions with similar temperature dependence of the superstructure peaks. In the case of SmBaMn$_2$O$_6$, the phase with $(h/4, k/4, l)_T$ and $(h/2, k/2, l/2)_T$ superstructure peaks adopt the orthorhombic SG *Pnam*. The addition of modes distortions from the irrep M4- to this SG gives rise to the subgroup *P2$_1$/n*. We have used this model of distortions to refine the pattern measured at 303 K obtaining good fits as can be seen in Table 3 and in the supplementary material (Fig. S3). The axes of the *P2$_1$/n* cell can be derived from the parent tetragonal structure with the following lattice vectors and origin shift: -$\mathbf{a}_T$-$\mathbf{b}_T$, -2$\mathbf{a}_T$+2$\mathbf{b}_T$, -2$\mathbf{c}_T$ and (-1, -1/2, -3/2) shift.

Table 3. Structural parameters of YBaMn$_2$O$_6$ obtained from Rietveld refinement at 303 K.

	Atom	Pos.	x	y	z	B_{iso}(Å^2)
SG: *P2$_1$/n*	Y1	*4e*	0.2520(5)	0.8819(1)	0.2545(2)	0.45(4)
	Y2	*4e*	0.2564(5)	0.8819(1)	0.7559(2)	0.70(5)
a = 5.52854(1) Å	Ba1	*4e*	0.2398(4)	0.8759(1)	0.0028(2)	1.42(3)
b = 11.04692(2) Å	Ba2	*4e*	0.2408(4)	0.8759(1)	0.5031(2)	0.19(2)
c = 15.23305(3) Å	Mn1	*4e*	0.7614(9)	0.3750(1)	0.6291(2)	0.48(1)
β = 90.3014(1)	Mn2	*4e*	0.7409(9)	0.8749(1)	0.6291(2)	0.48(1)
V = 930.321(4) Å^3	Mn3	*4e*	0.7589(9)	0.3750(1)	0.1289(2)	0.48(1)
	Mn4	*4e*	0.7340(9)	0.8749(1)	0.1289(2)	0.48(1)
R$_p$ (%) = 2.9	O1$_1$	*4e*	0.666(2)	0.9005(13)	0.2500(1)	0.85(9)
R$_{wp}$ (%) = 4.2	O1$_2$	*4e*	0.720(2)	0.9083(13)	0.7500(1)	0.85(9)
R$_{Bragg}$(%) = 2.3	O2$_1$	*4e*	-0.002(2)	-0.0111(12)	0.1418(6)	1.33(6)
χ^2 = 1.6	O2$_2$	*4e*	0.049(2)	-0.0150(12)	0.6430(6)	1.33(6)
	O2$_3$	*4e*	0.039(2)	0.4868(12)	0.1217(6)	1.33(6)
	O2$_4$	*4e*	0.009(2)	0.4941(12)	0.6229(6)	1.33(6)
	O2$_5$	*4e*	0.505(2)	0.2625(10)	0.1538(9)	1.33(6)
	O2$_6$	*4e*	0.495(2)	0.2643(10)	0.6446(9)	1.33(6)
	O2$_7$	*4e*	0.446(2)	0.7582(10)	0.1458(9)	1.33(6)
	O2$_8$	*4e*	0.435(2)	0.7600(10)	0.6526(9)	1.33(6)
	O3$_1$	*4e*	0.764(3)	0.8637(6)	-0.0067(7)	0.77(9)
	O3$_2$	*4e*	0.750(3)	0.8637(6)	0.5067(7)	0.77(9)

The *P2$_1$/n* structure decomposes into 60 distortion modes belonging to 12 irreps of the *P4/mmm* structure. When all possible amplitudes are refined, it is observed that a significant number of modes have very large errors. In these cases, the standard deviation exceeds or equals the absolute value of the distortion and we have canceled the corresponding modes, reducing the number of variables to be refined. The distortion modes that can be neglected are concentrated in the irreps S3, SM3 and Z4- (see Table 4). Curiously, these modes are absent in the distorted structure of the SmBaMn$_2$O$_6$, highlighting the great similarity between this compound and the YBMO. The structural data reported in Table 3 corresponds to the refinement of a total of 38 distortion modes.

Table 4. Summary of the mode decomposition with respect to its *P4/mmm* parent structure of the *P2₁/n* structure for YBMO at 303 K.

K-vector	Irrep	Direction	Dim.	Isotropic subgroup	Amplitude (Å)
(0,0,0)	GM1+	(a)	2	*P4/mmm*	0.53(1)
(0,0,0)	GM5+	(a,-a)	3	*C2/m*	0.10(1)
(1/4,1/4,0)	SM2	(0,a,a,0)	8	*Pbam*	1.30(2)
(1/4,1/4,0)	SM3	(0,a,a,0)	9	*Pbcm*	0.26(1)
(1/2,1/2,0)	M1-	(a)	1	*P4/nbm*	0.06(2)
(1/2,1/2,0)	M4-	(a)	1	*P4/nbm*	1.13(1)
(1/2,1/2,0)	M5-	(a,0)	6	*Pmma*	1.23(1)
(1/2,1/2,1/2)	A1+	(a)	2	*I4/mmm*	0.17(5)
(1/2,1/2,1/2)	A4+	(a)	3	*I4/mmm*	0.33(3)
(1/2,1/2,1/2)	A5+	(0,-a)	4	*Imma*	0.10(3)
(0,0,1/2)	Z4-	(a)	1	*P4₂/mmc*	0.0
(0,0,1/2)	Z5-	(a,0)	5	*Cmcm*	0.12(4)
(1/4,1/4,1/2)	S2	(0,a,-a,0)	6	*Cmca*	0.68(4)
(1/4,1/4,1/2)	S3	(0,a,a,0)	9	*Cmca*	0.03(1)

The mode decomposition of this structure is summarized in the Table 4 and the schematic representation of the global atomic shifts for the main irreps can be found in the supplementary information. As can be seen in the Table 4, the primary modes of this distortion belong to the irreps M4-, M5- and SM2 with global amplitudes well above 1 Å. The main contributions of the irreps M4- and M5- correspond to the abovementioned tilts of the MnO_6 octahedra. The distortion modes comprises in the irrep SM2 are responsible for the occurrence of $(h/4, k/4, l)_T$ superstructure peaks. Some of these modes acting on the Mn-O sublattice produce antiphase distortions along the orthorhombic *a* axis (*i.e.* in opposite directions for neighboring layers) leading to the duplication of the orthorhombic *b* axis. For this reason, some authors call them stripe distortions.[41] Regarding the basal oxygens, the distortions include rotation, asymmetric stretching, scissoring and twisting modes. They have the peculiarity that each mode only acts on half of the basal oxygens. The result

is that $O2_i$ (i=5-8; see Table 3) shifts in-phase along the *b* axis while $O2_j$ (j=1-4) are displaced in opposite directions along the *c* axis (see supplementary information).
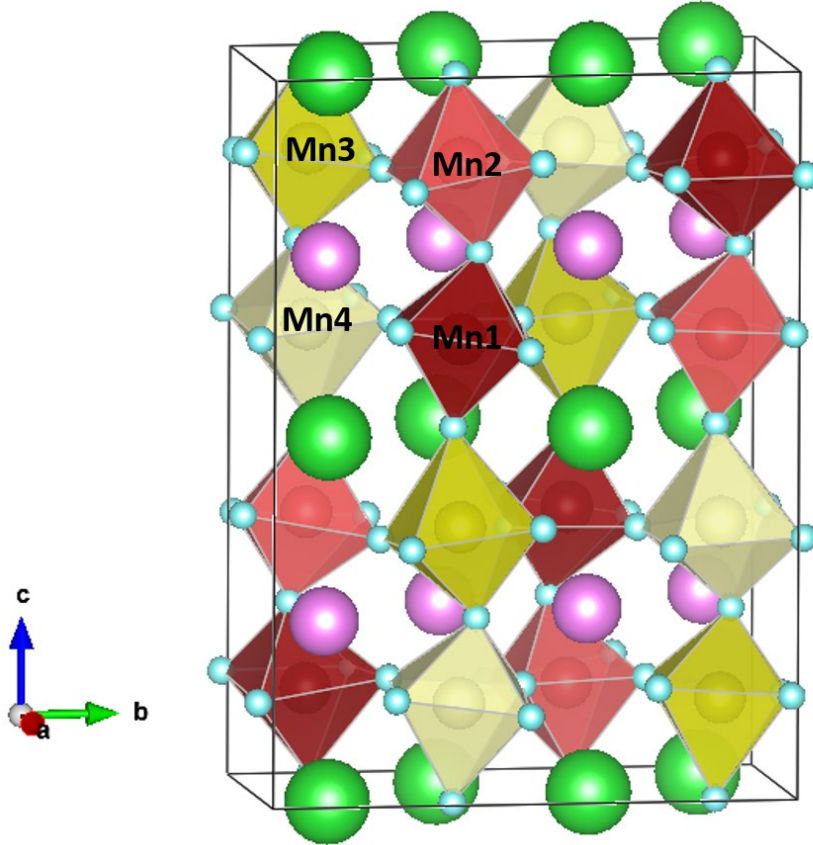

Figure 5. Crystal structure of $YBaMn_2O_6$ at 303 K. Big green, intermediate pink and small blue balls stand for Ba, Y and O atoms, respectively.

The rest of the modes have much smaller amplitudes but it is worth noting the contribution of two irreps: S2 and A4+. They are responsible for the doubling of the *c* axis because these distortions change their sign every two layers along this direction. Concerning the basal oxygens, the distortions of S2 modes are opposite to the ones indicated for SM2 ones. In this case, the $O2_i$ (i=5-8) shifts in opposite directions along the *c* axis while $O2_j$ (j=1-4) are displaced in the *ab* plane. The A4+ is associated to a breathing distortion acting on O2 and O3 atoms leading to a

checkerboard arrangement of compressed and expanded MnO_6 octahedra in the orthorhombic *ab* plane. The set of all these distortions gives rise to the structure represented in figure 5. There are four non-equivalent Mn sites with a small charge disproportionation between them. The BVS method yields the following valences: Mn1=+3.67(5), Mn2=+3.60(5), Mn3=+3.33(4) and Mn4=+3.35(4). Therefore, we have a quasi-bimodal charge distribution among the four sites with a charge difference between 0.25 and 0.34 e⁻. Mn3 and Mn4 can be grouped as $Mn^{3.5-\delta}$ (Mn1 and Mn2 as $Mn^{3.5+\delta}$), δ being ≈0.15. The charge disproportionation is well below the theoretical value of 1 e⁻ but is comparable to typical values observed in the CO transitions of related manganites.[9] It is noteworthy that the two types of MnO_6 octahedra are exchanged every two layers along the *c* axis (see Fig. 5). This feature was ascribed to an OO with the stacking sequence AABB. [14,20,24,25,31] In the present case, this explanation does not work as the distortions that produce the *P2₁/c* structure do not appear to be related to an OO. In fact, the distortion associated with an asymmetric stretching (Jahn-Teller like) is observed in the irrep M1- and its value is negligible (see Table 4).

Crystal structure of the LT-CO phase at 100 K (T_N>T). The $(h/2,\ k/2,\ l/2)_T$ superstructure peaks vanish below T_N while the $(h/4,\ k/4,\ l)_T$ ones remain in the pattern. The lattice parameters are again $2\sqrt{2}\mathbf{a}_T \times \sqrt{2}\mathbf{a}_T \times \mathbf{c}_T$ as at 473 K. However, the structural model using the SG *P2₁/c* does not account for the intensity of all diffraction peaks although the unit cell is still monoclinic. Looking at the list of possible structures driven by the combination of modes belonging to the M5-, M4- and SM irreps (see supplementary section), we observe a distorted structure with SG *P2₁* that presents distorted modes belonging to the irrep SM2, very strong in the previous phase. In addition, this SG is also a subgroup of the low temperature CO phase of $SmBaMn_2O_6$ compound which adopts the SG *P2₁am*.

Table 5. Structural parameters of YBaMn$_2$O$_6$ obtained from Rietveld refinement at 100 K.

	Atom	Pos.	x	y	z	B_{iso}(Å^2)
SG: *P2$_1$*	Y1	*2a*	-0.0068(5)	-0.0073(1)	0.0075(4)	0.18(3)
	Y2	*2a*	0.5174(5)	0.2573(1)	0.0160(3)	0.28(3)
a = 5.52772(1) Å	Ba1	*2a*	-0.0180(4)	-0.0007(1)	0.5070(3)	0.50(3)
b = 11.04256(2) Å	Ba2	*2a*	0.4982(4)	0.2507(1)	0.5059(3)	0.48(2)
c = 7.59032(2) Å	Mn1	*2a*	0.4816(6)	-0.0040(5)	0.2393(4)	0.25(1)
β = 90.3342(1)	Mn2	*2a*	0.5232(6)	0.4986(5)	0.2393(4)	0.25(1)
V = 463.306(2)Å^3	Mn3	*2a*	-0.0027(8)	0.2473(4)	0.2469(4)	0.25(1)
	Mn4	*2a*	0.0015(8)	0.7473(4)	0.2430(4)	0.25(1)
R$_p$ (%) = 3.2	O1$_1$	*2a*	0.410(2)	-0.0287(5)	0.0000(1)	0.85(9)
R$_{wp}$ (%) = 4.7	O1$_2$	*2a*	-0.036(2)	0.2787(5)	0.0000(1)	0.85(9)
R$_{Bragg}$(%) = 2.1	O2$_1$	*2a*	0.255(2)	0.1389(12)	0.2059(13)	0.83(6)
χ^2 = 1.9	O2$_2$	*2a*	0.319(2)	0.6308(12)	0.1985(13)	0.83(6)
	O2$_3$	*2a*	0.733(2)	0.3647 (12)	0.2609(13)	0.83(6)
	O2$_4$	*2a*	0.693(2)	0.8702(12)	0.2142(13)	0.83(6)
	O2$_5$	*2a*	0.744(2)	0.8950(10)	0.7829(13)	0.83(6)
	O2$_6$	*2a*	0.787(2)	0.3916(10)	0.7421(13)	0.83(6)
	O2$_7$	*2a*	0.191(2)	0.7582(10)	0.1458(9)	0.83(6)
	O2$_8$	*2a*	0.259(2)	0.7600(10)	0.6526(9)	0.83(6)
	O3$_1$	*2a*	0.500(3)	0.0115(6)	0.5000(7)	0.77(9)
	O3$_2$	*2a*	0.016(3)	0.2385(6)	0.5000(7)	0.77(9)

The axes of the *P2$_1$* cell is related to the parent tetragonal structure by the vectors $\mathbf{a}_T + \mathbf{b}_T$, $-2\mathbf{a}_T + 2\mathbf{b}_T$, and $\mathbf{c}_T$, without origin shift. We have obtained good fits using this model to refine the SXRPD pattern collected at 100 K. The fit can be seen in the supplementary information and the refined data are summarized in the Table 5. This distorted structure also decomposes into 60 distortion modes comprised in 12 irreps. This is a polar structure, so we have set the GM5- mode of the Ba atoms to zero as reference for the polar shifts. The refinement of the rest of the modes showed that some of them had small amplitudes with large standard deviations so we decided to cancel them. These modes were especially concentrated on the irreps M1+, GM4- and SM3. Finally, the refinement shown in the Table 5 is the result of refining a total of 43 distortion modes and the mode decomposition can be consulted in the Table 6. The schematic representation of the

atomic displacements for the main irreps are shown in the supplementary information and the representation of the crystal structure is shown in Fig. 6. As indicated in the Table 6, the primary modes belong to the M4-, M5- and SM2 irreps with global distortion amplitudes close or above 1 Å. As before, the distortion modes of M4- and M5- leads to the tilting of MnO_6 octahedra following the $a^-b^0c^-$ schema.[30] Again, the distortion modes belonging to SM2 irrep keep on promoting the formation of stripes in the *ab* plane. They consist of displacements along the *b* axis for Ba, Y, Mn and O1 atoms. These shifts are in antiphase for non-equivalent atoms (see supplementary information). The distortion produced in the O3 atoms is negligible while the O2 atoms are affected by the sum of several individual modes including rotation, twisting and asymmetric stretching. The result is a main shift of $O2_i$ (i=1,2,7,8) atoms along the b axis while $O2_j$ (j=3,4,5,6) are mainly displaced along the *ac* plane.

Table 6. Summary of the mode decomposition with respect to its *P4/mmm* parent structure of the *P2₁* structure for YBMO at 100 K.

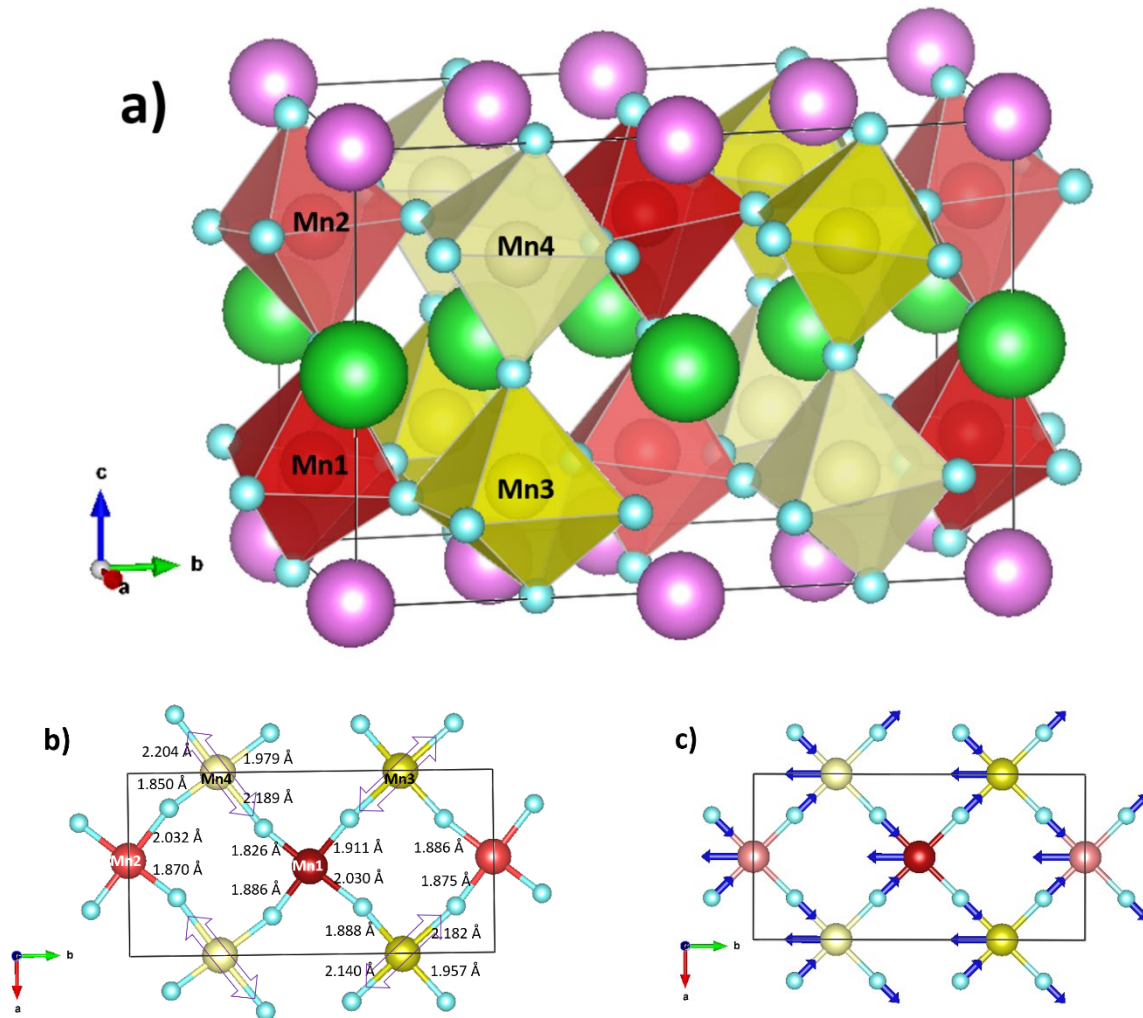| K-vector	Irrep	Direction	Dim.	Isotropic subgroup	Amplitude (Å)
(0,0,0)	GM1+	(a)	2	*P4/mmm*	0.33(1)
(0,0,0)	GM5+	(a,-a)	3	*C2/m*	0.05(1)
(0,0,0)	GM4-	(a)	1	*P-4m2*	0.0
(0,0,0)	GM5-	(a,-a)	7	*Amm2*	0.11(3)
(1/4,1/4,0)	SM2	(0,a,b,0)	16	*Pmc2₁*	1.13(2)
(1/4,1/4,0)	SM3	(0,a,b,0)	18	*Pmc2₁*	0.22(1)
(1/2,1/2,0)	M1-	(a)	1	*P4/nbm*	0.04(1)
(1/2,1/2,0)	M4-	(a)	1	*P4/nbm*	0.84(1)
(1/2,1/2,0)	M5-	(a,0)	6	*Pmma*	0.88(1)
(1/2,1/2,0)	M1+	(a)	1	*P4/mmm*	0.0
(1/2,1/2,0)	M4+	(a)	2	*P4/mmm*	0.27(2)
(1/2,1/2,0)	M5+	(0,-a)	5	*Pmna*	0.02(1)

Figure 6. (a) Crystal structure of $YBaMn_2O_6$ at 100 K. Big green, intermediate pink and small blue balls stand for Ba, Y and O atoms, respectively. (b) Top view showing the interatomic distances between Mn and O2 atoms. (c) Same top view showing the polar displacements of Mn and O2 atoms ascribed to the irrep GM5-.

The rest of the modes have significantly smaller amplitudes. Of them we can highlight those corresponding to M4+ irrep which consists of a breathing mode of O2 atoms. This distortion leads to a significant charge segregation among non-equivalent Mn sites. The BVS calculations

yield the valence values of +3.89(4), +3.86(4), +3.21(3) and +3.19(3) for Mn1, Mn2, Mn3 and Mn4, respectively. This results in a bimodal distribution of compressed and expanded MnO_6 octahedra with a charge segregation of $\Delta q=0.67(3)$ e$^-$. The distribution of the two octahedron types resembles a checkerboard pattern in the *ab* plane (see Fig. 6). Moreover, the *c* axis is no longer duplicated and the resulting structure is compatible with the AAAA stacking sequence of an OO phase as reported for related systems.[25] However, the active mode that can produce an asymmetric stretching compatible with a Jahn-Teller distortion in half of the MnO_6 octahedra (belonging to the irrep SM2) is not the main contribution in the global distortion of this structure. These octahedra are highly distorted and not rigid. Fig. 6(b) shows the distribution of Mn-O2 bond lengths. Compressed octahedra have three short and one long Mn-O distances whereas the expanded ones exhibit a range of distances that includes two very long, one intermediate and one short. The two very long distances are oriented perpendicularly between the two types of expanded octahedra in the ab plane (see Fig. 6(b)) and can lead to features in resonant x-ray scattering experiments similar to an OO phase but keep in mind that all octahedra are anisotropic and can present resonant contributions.

This is a polar structure and by symmetry of the SG allows spontaneous polarization along the unique *b* axis. There are three irreps whose isotropic subgroup are non-centrosymmetric (see table VI). Our refinements show a negligible contribution from the individual mode of the irrep GM4-. On the other hand, it is noteworthy that the order parameters of the irrep SM2 are not equal in this phase (*a* and *b* in Table 6) giving rise to a polar isotropic subgroup. The amplitude difference in the shifts of non-equivalent sites breaks the symmetry center but the global distortion produced by this irrep are located along the *a* axis and does not lead to a ferroelectric component along the *b* axis. Finally, the distortions ascribed to the irrep GM5- are compatible with a ferroelectric

component along the *b* axis. In our structural model we are set to zero the contribution of Ba atoms as reference. Our refinements yield negligible displacements for Y and apical oxygens. However, it reveals significant shifts for Mn and basal oxygens as can be seen in Fig. 6(c). The Mn atoms are shifted along the y-direction while an asymmetric stretching mode of the O2 atoms lead to a net component along the b axis in opposite direction to the Mn displacement. Calculation of the theoretical displacive-type ferroelectric polarization[28] yield a value of 4.3 µC cm^{-2} for this phase. This value is somewhat greater than that calculated in the related $SmBaMn_2O_6$,[28] which suggests an increase of the polarization as the distortion of the crystal structure increases in agreement with theoretical predictions.[42]

Temperature dependence of the crystallographic properties. In order to compare the data of the different phases, the cell parameters were converted into the values corresponding to the high temperature phase (SG *C2/m*). In this way, *a* was multiplied (and *b* divided) by $\sqrt{2}$ in the *P2$_1$* and *P2$_1$/n* phases. The same transformation was performed in the *P2$_1$/c* phase after interchanging *a* and *c* axes. Finally, the *c* axis was divided by 2 in the *P2$_1$/n* cell. Figure 7(a) shows the temperature dependence of the resulting lattice parameters for the YBMO compound between 100 and 603 K. The temperature evolution of these parameters is reminiscent of those observed in isostructural compounds.[18,28] It is characterized by strong changes at T$_1$ that coincides with the corresponding anomaly indicated in the magnetic measurements (see Fig. 1). In this transition there is a huge expansion of the *b* axis while a strong shrinkage is produced for the *a* and *c* axes. This behavior was previously reported at this transition which curiously involves a small anomaly in the electrical resistivity of the compound.[29] It is a first order transition with hysteretic behavior and coexistence of the two phases in a temperature range of ~30 K. This observation agrees with the fact that P2$_1$/c is not a direct subgroup of *C2/m*. At this transition, a sharp decrease in the

monoclinic distortion is also observed, reflected in a sudden decrease of the β-angle that can be seen in figure 7(b). In addition, there is a severe expansion of the unit cell volume at T_1 as can be seen in Fig 7(c). This could be favored by the electron localization in agreement with the Virial theorem for a first-order metal-insulator transitions.[43] It is noteworthy that the big changes observed in the YBMO compound differ from those shown by the $SmBaMn_2O_6$ compound where there is a large expansion of the *ab* plane coupled with a decrease of the *c* axis.[28]

At lower temperatures and coinciding with T_2, there is a turning point in the temperature dependence on the three parameters. It is a downturn point for *ab* plane and an upturn point for the *c* axis. This small anomaly coincides with the occurrence of the ($h/4$, $k/4$, $l/2$) superstructure peaks and with the strong metal-insulator-like transition reported by Nakajima *et al.*[29] Given the similarities observed with the $SmBaMn_2O_6$ (identical superstructure peaks) we have called this phase as HT-CO. At this temperature, an upturn point is also observed in the evolution of the monoclinic distortion, but curiously, no significant changes are observed in the evolution of the unit cell volume. In the *P2₁/n* phase, the volume of the cell contracts continuously due mainly to the contraction of the *c* axis since the *ab* plane experience less variation with temperature. On cooling, the monoclinic distortion in this phase increases remarkably from ~365 K and undergoes an abrupt jump at T_N, marking the transition to the low temperature phase *P2₁*. The magnetic and structural transitions seem to be coupled and it is a first order transition characterized by a large hysteresis between cooling and heating conditions. The transition is also characterized by a sharp rise of the *a* and *b* axis coupled to a similar decrease in the *c* axis. These changes are abrupt but are dwarfed when compared to the large changes observed at T_1. We have renamed this phase as LT-CO since, as occurred in the $SmBaMn_2O_6$ compound, the ($h/4$, $k/4$, $l/2$) superstructure peaks disappear but the ($h/4$, $k/4$, l) ones remain.
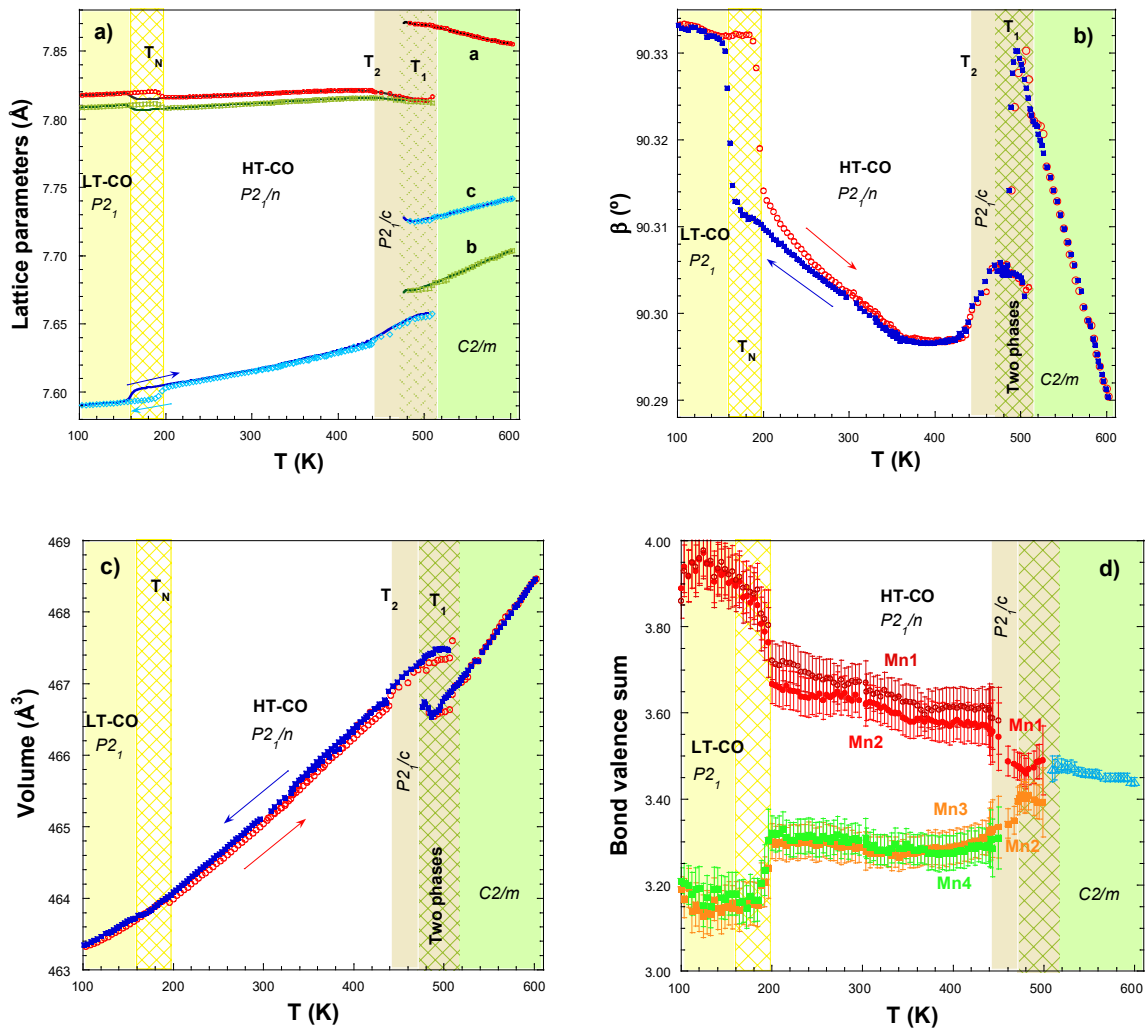
Figure 7. (a) Temperature dependence of the lattice parameters (a), β-angle (b) and unit cell volume (c) for YBaMn$_2$O$_6$ in the heating and cooling ramp between 100 and 603 K. The lattice parameters are referred to the high temperature phase. (d) Temperature dependence of the valences for the different Mn sites in each phase of the YBaMn$_2$O$_6$ obtained from BVS calculation in the patterns collected in heating conditions from 100 K up to 603 K.

Next, in order to study the interplay between electronic localization and CO, we have monitored the temperature dependence of the Mn valence in the different phases by means of the BVS method.[40] The results can be seen in the Fig. 7(d). The high temperature phase (SG $C2/m$)

29

has a single non-equivalent site for Mn atoms and as abovementioned, BVS yields a value of +3.41(1) at 603 K. Upon cooling, this value increases up to reach +3.48(1) just at T_1. Below this transition temperature, the Mn site splits into two non-equivalent sites in the $P2_1/c$ phase. However, Δq between the two sites remains small with values ranging between 0.05 and 0.12 e⁻ and Δq slightly increases when approaching T_2. Below this second transition temperature, there are four non-equivalent Mn sites although BVS calculations clearly differentiate two pairs of Mn atoms. The Mn1 and Mn2 atoms in the compressed octahedra have higher valence values that moreover increases as the temperature decreases. Thus, the value for Mn1 ranges between +3.60 and +3.71 while the range is between +3.56 and +3.66 for Mn2. In the case of the expanded octahedra, the valence values for Mn3 and Mn4 range between +3.28 and +3.33 and their temperature dependence is lower. Accordingly, Δq continuously increases with decreasing temperature in the HT-CO phase achieving a value of $\Delta q \sim 0.4$ e⁻ just above T_N. The LT-CO phase also has four non-equivalent sites for Mn atoms and the separation in two pairs of Mn atoms is maintained, widening further the charge segregation between pairs that reaches values $\Delta q \sim 0.7$ e⁻. Overall, the temperature evolution of Δq is opposite to that observed in $SmBaMn_2O_6$ where the higher values of Δq were observed in the HT-CO phase and this might be related to the high degree of structural distortion produced by the small Y^{3+} cation and the absence of FM correlations.[28] The simultaneous occurrence of electric and magnetic transitions classified this compound as a type II multiferroic[44] and a significant magnetoelectric coupling at the transition temperature can be anticipated in the polar and presumably ferroelectric LT-CO phase.

CONCLUSIONS

Successive phase transitions on cooling of YBMO compound lead to a rich variety of crystal structures. Competition between octahedral rotations, charge segregation among Mn sites and asymmetric stretching distortions could account for the stabilization of different distorted structures. Four successive distorted structures have been described respect to the ideal tetragonal structure using the symmetry-adapted distortion mode formalism.[35] Initially, antiphase tilts of the MnO_6 octahedra following the schema $a^-b^0c^-$ relieve the structural strain produced by the small size of the Y^{3+} cation. Due to the layered ordering of the Y^{3+} and Ba^{2+} cations, the MnO_6 octahedra do not stay rigid when rotating and show a strong distortion. The resulting structure is monoclinic with SG *C2/m*. In this phase, the Mn atoms have a mixed valence state close to the theoretical value of 3.5.

At $T_1 \approx 495\text{-}512$ K, a structural transition is mediated by the condensation of modes belonging to the irrep SM2 and it is characterized by a great change in the lattice parameters. These modes stabilize a checkerboard pattern in the *ab* plane (considering the reference axes of the LT-CO phase) but the charge difference between the two non-equivalent Mn sites remain small. At $T_2 \approx 450\text{-}460$ K, the contribution of additional distortion modes from S2 and A4+ irreps leads to a duplication of the *c* axis and the occurrence of $(h/4, k/4, l/2)_T$ superstructure peaks. The new cell has four non-equivalent sites for Mn atoms but they are grouped in two pairs preserving the checkerboard arrangement in the *ab* plane though their positions are exchanged every two layers of MnO_6 octahedra along the *c* axis. The doubling of this axis is ascribed to the AABB stacking sequence of the OO for this and related compounds.[14,20,24,25,31] However, our refinements clearly unveil than Mn-O_{basal} distances are composed by three short and one long bond lengths in the compressed atoms and the opposite distribution in the expanded ones. The latter disagree with the formation of an OO of e_g ($3d_{x^2-z^2}/3d_{y^2-z^2}$) orbitals. Moreover, the charge segregation between

different pairs of Mn atoms achieve the value of $\Delta q \approx 0.4$ e$^-$ in this phase, well below the theoretical value of one charge unit for a complete CO.

Coupled to the magnetic transition at T_N there is another structural transition. The disappearance of modes associated to S2 and A4+ irreps ends the duplication of the c axis. The low temperature cell is polar with SG *P2$_1$* and it also contains four non-equivalent Mn sites. The coherence of the checkerboard pattern along the c axis is established and corresponds to the AAAA stacking sequence of an OO. In this case, a Jahn-Teller-like distortion in the two expanded MnO$_6$ octahedra is produced due to enhancement of an asymmetric stretching mode ascribed to the SM2 irrep. This structure is polar and allows ferroelectricity in the direction of the unique axis. There are three irreps whose isotropy subgroup is non-centrosymmetric. Our refinements disclose a negligible contribution from the mode belonging to the GM4- irrep while the distortions produced by the modes belonging to the SM2 irrep comprise atom shifts in opposite directions along the *ac* plane that lead to an ordered sequence of stripes perpendicular to the *b* axis without a net polarization. The ferroelectricity is associated to the modes from the GM5- irrep and the polar shifts correspond to the Mn and O$_{basal}$ atoms that display a net displacement in opposite directions along the *b* axis.

The structures presented here allow us to account for all the superstructure peaks observed in the diffraction patterns of each phase for the first time. In addition, the mode analysis permits us to know the sequence of distortions that lead to the different phase transitions and their relationship with other layered manganites.

Supporting Information. It contains: (i) a table with the list of distorted structures from the parent tetragonal cell and with active points (½, ½, 0) and (¼, ¼, 0); (ii) Rietveld plots at four

selected temperatures: 603, 473, 303 and 100 K; (iii) tables with the mode decomposition respect to the parent tetragonal cell for the distorted structures at 603, 473, 303 and 100 K; (iv) schematic representation of the distortion modes ascribed to the main irreps to describe the different structural phases at 303 and 100 K respect to the ideal undistorted *P4/mmm* phase. This supporting information is available free of charge at http://pubs.acs.org***

AUTHOR INFORMATION

Corresponding Author

*Javier Blasco.

Instituto de Nanociencia y Materiales de Aragón (INMA), CSIC-Universidad de Zaragoza, and Departamento de Física de la Materia Condensada, Universidad de Zaragoza, C/ Pedro Cerbuna 12, 50009 Zaragoza, (Spain). E-mail:jbc@unizar.es

ORCID

Javier Blasco: 0000-0002-9706-3272

Gloria Subías: 0000-0002-9029-1977

José Luis García-Muñoz: 0000-0002-4174-2794

François Fauth: 0000-0001-9465-3106

Joaquín García :

Author Contributions

The manuscript was written through contributions of all authors. All authors have given approval to the final version of the manuscript.

Notes

The authors declare no competing financial interest.

ABBREVIATIONS

CO, Charge Ordering; OO, Orbital Ordering; FM, FerroMagnetic; AFM, AntiFerroMagnetic; R, Rare earth; YBMO, $YBaMn_2O_6$; RT, Room Temperature; SG, Space Group; SXRPD, Synchrotron X-Ray Powder Diffraction; MYTHEN, Microstrip sYstem for Time-rEsolved experimeNts; NIST, National Institute of Standards and Technology; SQUID, Superconducting QUantum Interference Device; NPD, Neutron Powder Diffraction; TEM, transmission electron microscopy; irrep, irreducible representation; HT-CO, High Temperature Charge Ordering; LT-CO, Low Temperature Charge Ordering.

REFERENCES

(1)   Coey, J. M. D.; M. Viret, M.; von Molnar, S. Mixed-valence manganites. *Adv. Phys.* **1999**, *48(2)*, 167-293.

(2)   Tokura, Y. Critical features of colossal magnetoresistive manganites. *Rep. Prog. Phys*. **2006**, *69(3)*, 797-, and references therein.

(3)   Subías, G.; García, J.; Blasco, J.; Proietti, M.G. Local structure at the manganese site in mixed-valence manganites. *Phys. Rev. B* **1998**, *57(2)*, 748-754.

(4)   Zhang, Y.; Zhao, H.; Du, Z.; Świerczek, K.; Li, Y. High-Performance SmBaMn$_2$O$_{5+\delta}$ Electrode for Symmetrical Solid Oxide Fuel Cell. *Chem. Mat.* **2019**, *31*, 3784-3793.

(5)   Motohashi, T; Takahashi, T; Kimura, M; Masubuchi, Y.; Kikkawa, S; Kubota, Y.; Kobayashi, Y.; Kageyama, H.; Takata, M.; Kitagawa, S.; *et al*. Remarkable oxygen intake/release of BaYMn$_2$O$_{5+\delta}$ viewed from high-temperature crystal structure. *J. Phys. Chem. C* **2015**, *119*, 2356−2363

(6)   Volkov, N. V. Spintronics: manganite-based magnetic tunnel structures. *Physics-Uspekhi,* **2012**, *55(3)*, 250-269.

(7)   Phan, M. H.; Yu, S. C. Review of the magnetocaloric effect in manganite materials. *J. Mag. Mag. Mat.* **2007**, *308*, 325-340.

(8)   Tokura, Y.; Nagaosa, N. Orbital Physics in Transition-Metal Oxides. *Science*. **2000**, *288*, 462-468.

(9)   Radaelli, P.; Cox, P. E.; Marezio, M.; Cheong, S. W.; Schiffer, P. E.; Ramirez, A. P. Simultaneous Structural, Magnetic, and Electronic Transitions in La$_{1−x}$Ca$_x$MnO$_3$ with x=0.25 and 0.50. *Phys Rev. Lett.* **1995**, *75(24)*, 4488.

(10)   Tomioka Y.; Asamitsu, A.; Moritomo, Y.; Kuwahara, H.; Tokura, Y. Collapse of a Charge-Ordered State under a Magnetic Field in Pr$_{1/2}$Sr$_{1/2}$MnO$_3$. *Phys. Rev. Lett.* **1995,** *74*, 5108.

(11)   Lafuerza, S.; García, J.; Subías, G.; Blasco, J.; Glatzel, P. High-resolution Mn K-edge x-ray emission and absorption spectroscopy study of the electronic and local structure of the three different phases in $Nd_{0.5}Sr_{0.5}MnO_3$. *Phys. Rev. B.* **2016**, *93*, 205108.

(12)   Ueda, Y.; Nakajima, T. The A-site ordered manganese perovskite and its colossal magnetoresistance. *Prog. Sol. State Chem.* **2007**, *35*, 397-406.

(13)   Nakajima, T.; Kageyama, H.; Yoshizawa, H.; Ueda, Y. Structures and Electromagnetic Properties of New Metal-Ordered Manganites: $RBaMn_2O_6$ (R = Y and Rare-Earth Elements). *J. Phys. Soc. Jap.* **2002**, *71*, 2843-2846.

(14)   Arima, T.; Akahoshi, D.; Oikawa, K.; Kamiyama, T.; Uchida, M.; Matsui, Y.; Tokura, Y. Change in charge and orbital alignment upon antiferromagnetic transition in the A-site-ordered perovskite manganese oxide $RBaMn_2O_6$ (R=Tb and Sm). *Phys. Rev. B.* **2002**, *66*, 140408(R).

(15)   Benedek, N. A.; Rondinelli, J. M.; Djana, H.; Ghosez, P.; Lightfoot, P. Understanding ferroelectricity in layered perovskites: new ideas and insights from theory and experiments. *Dalton Trans.* **2015**, *44*, 10543-10558.

 (16)   Nakajima, T.; Tsuchiya, T.; Daoudi, K.; Ichihara, M.; Ueda, Y.; Kumagai, T. Epitaxial A-site ordered perovskite manganite $SmBaMn_2O_6$ film on $SrTiO_3$(001): fabrication, structure, and physical property. *Chem. Mater.* **2007**, *19*, 5355-5362.

 (17)   Millange, F.; Caignaert, V.; Domengès, B.; Raveau, B.; Suard, E. Order-Disorder Phenomena in New $LaBaMn_2O_{6-x}$ CMR Perovskites. Crystal and Magnetic Structure. *Chem. Mater.* **1998**, *10*, 1974-1983.

(18)   Blasco, J.; Subías, G.; Sanjuán, M. L.; García-Muñoz, J. L.; Fauth, F.; García, J. Structure and phase transitions in A-site ordered RBaMn$_2$O$_6$ (R = Pr, Nd) perovskites with a polar ground state. *Phys. Rev. B*. **2021**, *103*, 064105.

(19)   Nakajima, T.; Kageyama, H.; Yoshizawa, H.; Ohoyama, K.; Ueda, Y. Ground State Properties of the A-site Ordered Manganites, RBaMn$_2$O$_6$ (R = La, Pr and Nd). *J. Phys. Soc. Jap*. **2003**, *72*, 3237-3242.

(20)   Akahoshi, D.; Okimoto, Y.; Kubota, M.; Kumai, R.; Arima, T.; Tomioka, Y.; Tokura, Y. Charge-orbital ordering near the multicritical point in A-site ordered perovskites SmBaMn$_2$O$_6$ and NdBaMn$_2$O$_6$. *Phys. Rev. B*. **2004**, *70*, 064418.

(21)   Yamada, S.; Sagayama, H.; Higuchi, K.; Sasaki, T.; Sugimoto, K.; Arima, T. Physical properties and crystal structure analysis of double-perovskite NdBaMn$_2$O$_6$ by using single crystals. *Phys. Rev. B* **2017**, *95*, 035101.

(22)   Nakajima, T.; Yoshizawa, H.; Ueda, Y. A-site Randomness Effect on Structural and Physical Properties of Ba-based Perovskite Manganites. *J. Phys. Soc. Jpn*. **2004**, *73*, 2283-2292.

(23) Y. Ueda and T. Nakajima. Novel structures and electromagnetic properties of the A-site-ordered/disordered manganites RBaMn$_2$O$_6$/R$_{0.5}$Ba$_{0.5}$MnO$_3$ (R = Y and rare earth elements) *J. Phys.:Condens. Matter*. **2004**, *16*, S573-S583.

(24)   Uchida, M.; Akahoshi, D.; Kumai, R.; Tomioka, Y.; Arima, T.; Tokura, Y.; Matsui, Y. Charge/Orbital Ordering Structure in Ordered Perovskite Sm$_{1/2}$Ba$_{1/2}$MnO$_3$. *J. Phys. Soc. Jpn*. **2002**, *71*, 2605-2608.

(25)   García-Fernández, M.; Staub, U.; Bodenthin, Y.; Lawrence, S. M.; Moulders, A. M.; Buckley, C. E.; Weyeneth, S.; Pomjakushina, E.; Conder, K. Resonant soft x-ray powder diffraction study to determine the orbital ordering in A-site-ordered $SmBaMn_2O_6$. *Phys. Rev. B* **2008**, *77*, 060402 (R).

(26)   Morikawa, D.; Tsuda, K.; Maeda, Y.; Yamada, S.; Arima, T. Charge and Orbital Order Patterns in an A-Site Ordered Perovskite-Type Manganite $SmBaMn_2O_6$ Determined by Convergent-Beam Electron Diffraction. *J. Phys. Soc. Jap*. **2012**, *81*, 093602.

(27)   Kageyama, H.; Nakajima, T.; Ichira, M.; Ueda, Y.; Yoshizawa, H.; Ohoyama, K. New Stacking Variations of the Charge and Orbital Ordering in the Metal-Ordered Manganite $YBaMn_2O_6$. *J. Phys. Soc. Jap.* **2003**, *72*, 241-244.

(28)   Blasco, J.; Subías, G.; García-Muñoz, J. L.; Fauth, F.; Sánchez, M. C.; García, J. Symmetry mode analysis of distorted polar/non-polar structures in A-site ordered $SmBaMn_2O_6$ perovskite. *Phys. Rev. B* **2021**, *103*, 214110.

(29)   Nakajima, T.; Kageyama, H.; Ueda, Y. Successive phase transitions in a metal-ordered manganite perovskite $YBaMn_2O_6$. *J. Phys. Chem. Sol.* **2002**, *63*, 913-916.

(30)   Glazer, A. M. Simple ways of determining perovskite structures. *Acta Crystallogr. Sect. A*. **1975**, *31*, 756-762.

(31)   Nakajima, T.; Kageyama, H.; Ichihara, M.; Ohoyama, K.; Yoshizawa, H.; Ueda, Y. Anomalous octahedral distortion and multiple phase transitions in the metal-ordered manganite $YBaMn_2O_6$. *J. Sol. State Chem*. **2004**, *177*, 987-999.

(32)   Williams, A. J.; Attfield, J. P.; Redfern, S. A. T. High-temperature orbital, charge, and structural phase transitions in the cation-ordered manganites $TbBaMn_2O_6$ and $YBaMn_2O_6$. *Phys. Rev. B.* **2005,** 72, 184426.

(33)   Williams, A. J.; Attfield, J. P., Ferro-orbital order in the charge- and cation-ordered manganite $YBaMn_2O_6$. *Phys. Rev. B* **2005**, *72*, 024436.

(34)   Rodríguez-Carvajal, J. Recent advances in magnetic structure determination neutron powder diffraction. *Phys. B* **1993**, *192*, 55−69. Available at https://www.ill.eu/sites/fullprof/

(35)   Pérez-Mato, J. M.; Orobengoa, D.; Aroyo, M. I. Mode Crystallography of distorted structures. *Acta Crystallogr., Sect. A:Found. Crystallogr*. **2010**, *66*, 558−590.

(36)   Campbell, B. J.; Stokes, H. T.; Tanner, D. E.; Hatch, D. M. ISODISPLACE: a web-based tool for exploring structural distortions. *J. Appl. Crystallogr*. **2006**, *39*, 607-614. Available at ISOTROPY Software Suite, iso.byu.edu.

(37)   Momma, K.; Izumi, F. VESTA 3 for three-dimensional visualization of crystal, volumetric and morphology data. *J. Appl. Crystallogr*. **2011**, *44*, 1272-1276.

(38)   Fauth, F.; Peral, I.; Popescu, C.; Knapp, M. The new Material Science Powder Diffraction beamline at ALBA Synchrotron. *Powder Diffr*. **2013**, *28*, S360-S370.

(39)   Aroyo, M.; Kirov, A.; Capillas, C.; Perez-Mato, J.; Wondratschek, H. Bilbao Crystallographic Server II: Representations of crystallographic point groups and space groups. *Acta Crystallogr. Sect. A* **2006**, *62*, 115-128.

(40)   Brown, I. D.; Altermatt, D. Bond-valence parameters obtained from a systematic analysis of the Inorganic Crystal Structure Database. *Acta Crystallogr. Sect. B* **1985**, *41*, 244-247.

(41)   Nowadnick, E. A.; He, J.; Fennie, C. J. Coupled structural distortions, domains, and control of phase competition in polar $SmBaMn_2O_6$. *Phys. Rev. B* **2019**, *100*, 195129.

(42) Yamauchi, K. Theoretical Prediction of Multiferroicity in $SmBaMn_2O_6$. J. Phys. Soc. Jpn. **2013**, *82*, 043702.

(43)   Goodenough, J. B. Colossal Magnetoresistance in $Ln_{1-x}A_xMnO_3$ Perovskites. *Aust. J. Phys.* **1999**, *52*, 155-186.

(44)   Khomskii, D. Classifying multiferroics: Mechanisms and effects. *Physics* **2009**, *2*, 20.

TOC graphic.
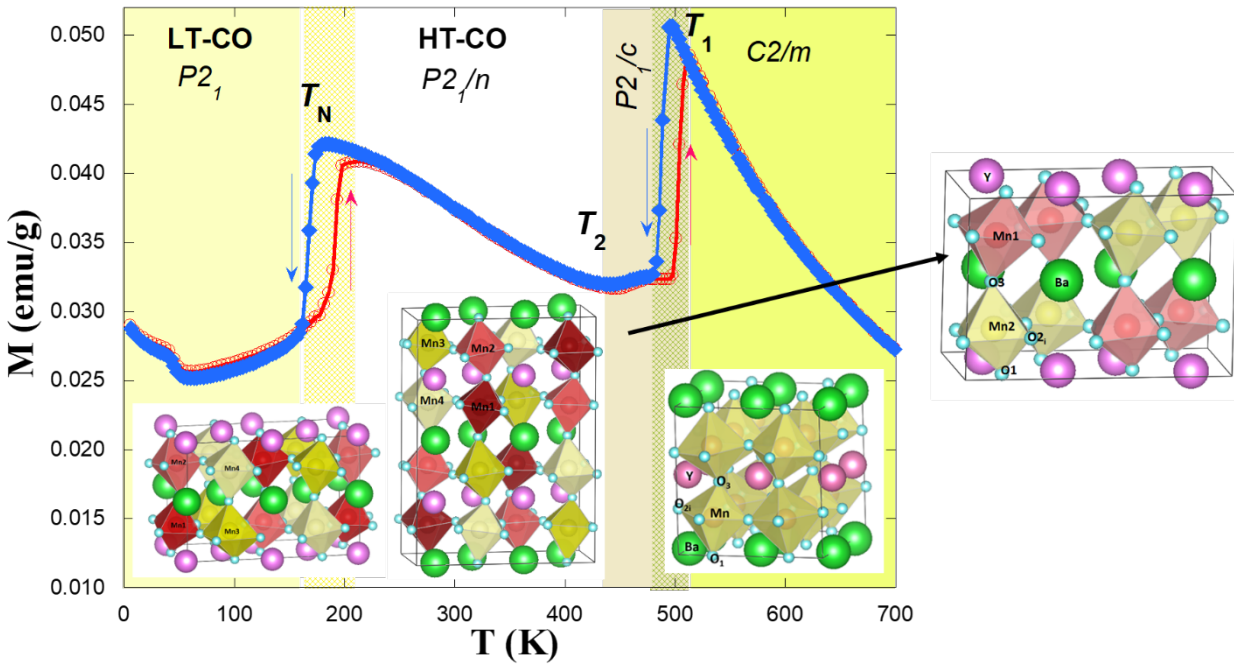
YBaMn$_2$O$_6$ undergoes three structural transitions upon cooling. These transitions give rise to clear anomalies in the magnetization curve with thermal hysteresis. At high temperature, SBMO adopts a monoclinic structure with a single site for Mn atoms. At T$_1$, this site splits into two non-equivalent sites giving rise to a dimer distribution. At T$_2$, a new transition leads to four non-equivalent Mn sites with a checkerboard charge segregation in the *ab*-plane whose distribution is swapped along the *c*-axis every two layers and keeping the inversion center. Finally, a new transition at T$_N$ breaks the symmetry center but preserves the checkerboard arrangement of Mn sites resulting in a polar phase.